Elliptical micropillars for efficient generation and detection of coherent acoustic phonons

C. Xiang,[†] A. Rodriguez,[†] E.R. Cardozo de Oliveira,[†] L. Le Gratiet, I. Sagnes, M. Morassi, A. Lemaître, and N.D. Lanzillotti-Kimura[*]

Université Paris-Saclay, CNRS, Centre de Nanosciences et de Nanotechnologies (C2N), 10 Boulevard Thomas Gobert, 91120 Palaiseau, France

(Received 24 October 2023; revised 8 June 2024; accepted 17 June 2024; published 26 July 2024)

Coherent acoustic phonon generation and detection assisted by optical resonances are at the core of efficient optophononic transduction processes. However, when one is dealing with a single optical resonance, the optimum generation and detection conditions occur at different laser wavelengths, i.e., different detunings from the cavity mode. In this work, we theoretically propose and experimentally demonstrate the use of elliptical micropillars to reach these conditions simultaneously at a single wavelength. Elliptical micropillar optophononic resonators present two optical modes with orthogonal polarizations at different wavelengths. By using a cross-polarization-scheme pump-probe experiment, we exploit the mode splitting and couple the pump beam to one mode while the probe is detuned from the other mode. In this way, at a particular micropillar ellipticity, the phonon-generation and phonon-detection processes are both enhanced. We report an enhancement of the coherent-phonon-generation-detection process by a factor of approximately 3.1 when comparing the highest achievable signals from elliptical and circular micropillars. Our findings constitute a step forward in tailoring light-matter interaction for more-efficient ultrahigh-frequency optophononic devices.

DOI: 10.1103/PhysRevApplied.22.014069

I. INTRODUCTION

The efficient manipulation of gigahertz acoustic phonons at the nanoscale is crucial for transforming various technological applications, from quantum information to data processing [1–3]. For instance, the long phonon lifetimes and short wavelengths make them good candidates for information carriers and quantum memories. The coupling of gigahertz acoustic phonons with superconducting qubits [4–6] or cavity exciton-polaritons [7,8], with use of gigahertz bulk-acoustic-wave resonators, exemplifies the potential of the field. Optophononic resonators based on GaAs/AlAs semiconductor microcavities, on the other hand, offer versatile platforms reaching frequencies up to a few terahertz [9–11]. The resonant frequency of acoustic phonons in the vertical direction depends on layer thicknesses, controlled through advanced techniques such as molecular-beam epitaxy [12]. Tailoring the optophononic properties of these resonators by defining 3D structures, such as micropillars, enhances light-matter interactions due to the lateral confinement that localizes the optical and acoustic fields [13–15]. Additionally, these systems allow the integration of acoustic resonators with other solid-state platforms, such as exciton-polaritons or single-photon sources, when one is defining quantum wells or quantum dots at the cavity spacer [16–18]. However, efficient transduction for optimum phonon generation and detection at the nanoscale remains a major challenge. This issue has been explored in acoustoplasmonics [19–24], and recently the use of circularly polarized light with plasmonic structures having chiral geometry to selectively enhance phonon generation and detection was proposed [25]. In this work, we present an alternative strategy based on semiconductor micropillars that simultaneously confine near-infrared light and acoustic phonons.

Manipulation of ultrahigh-frequency acoustic phonons usually requires all-optical experiments, such as time-domain Brillouin scattering [26–28]. In microcavity optophononic resonators, the roadblock arises from the fact that the phonon-generation process is most efficient when the excitation laser matches the optical mode resonance, while phonon detection, linked to optical reflectivity changes due to changes in the refractive index, is most sensitive at the slope of the optical mode [29–31]. This limitation can be overcome by the use of two lasers slightly detuned so as to reach the optimum

[*]Contact author: daniel.kimura@c2n.upsaclay.fr
[†]These authors contributed equally to this work.

condition [22,32]. While an effective and straightforward strategy, this solution requires two laser oscillators. Another approach is to change the angle of incidence of the excitation laser so that the in-plane component of the optical dispersion relation leads to a different resonant mode [29]. Although successful in planar microcavities based on distributed Bragg reflectors (DBRs), this technique is not feasible with micropillars due to lateral confinement constraints. To date, in the case of micropillars, no phonon-enhancement strategies have been proposed, except the integration of pillar microcavities with single-mode fibers, enabling long-term stabilization and reproducible plug-and-play experiments [33].

In this scenario, elliptical micropillars emerge as promising options for increasing device efficiency. Their elliptical shape induces birefringence, causing the confined optical mode to split into two nondegenerate polarized modes aligned with the micropillar axes [34–36]. The size and ellipticity of the micropillars determine the mode splitting. Elliptical micropillars have been used to improve the emission of single-photon sources based on quantum dots embedded in a microcavity spacer [37–40]. Elliptical micropillars have recently been used to manipulate the polarization selection rules of spontaneous (incoherent) Brillouin scattering [41]. A polarization-based spectral filtering of the laser was achieved by use of the wavelength-dependent rotation of polarization induced by the elliptical micropillars. In this article, we theoretically propose and experimentally demonstrate how to simultaneously enhance the coherent phonon generation and detection. In contrast to previous reports [41], we enhance the *coherent* phonon signals, and no rotation of polarization is involved. Through experimentation with micropillars of different ellipticities, we establish that an optimum ellipticity significantly enhances the phonon-generation-detection process.

II. METHODS

A. Experimental details

The structures studied are based on an optophononic microcavity grown on a (001)-oriented GaAs substrate by molecular-beam epitaxy. It consists of two DBRs enclosing a $\lambda/2$ GaAs spacer [Fig. 1(a)] [16,41]. The

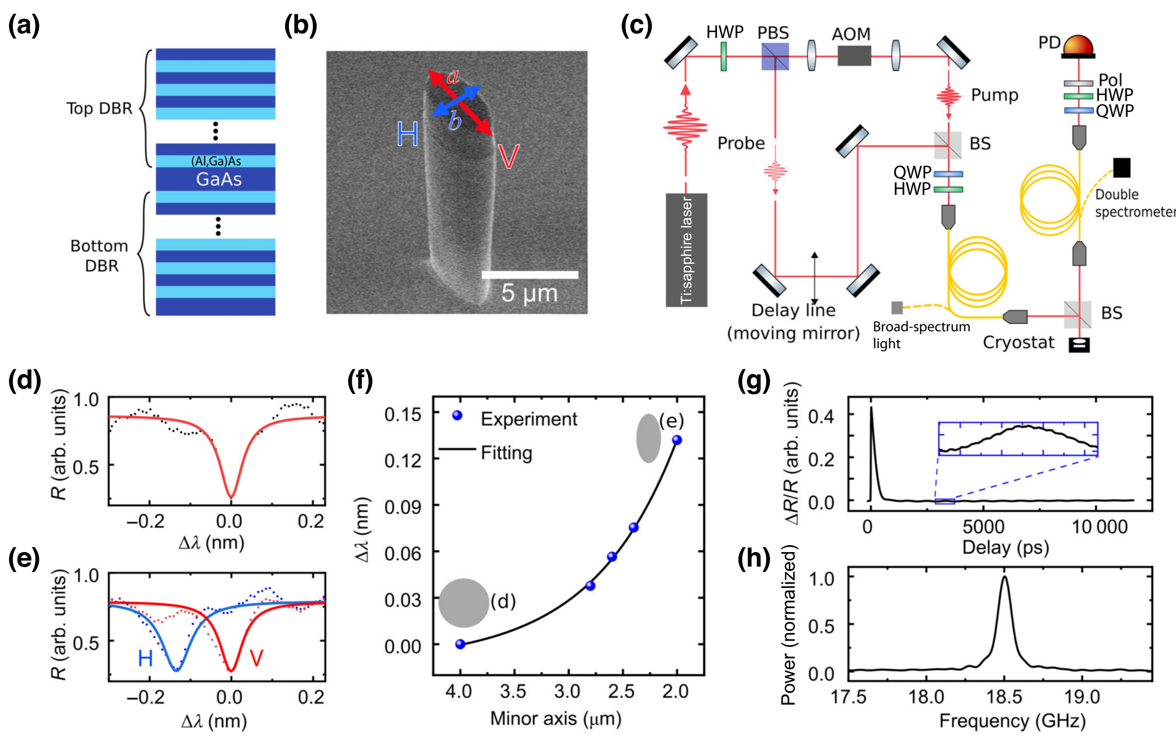

FIG. 1. (a) Vertical structure of the micropillars. Dark (light) blue corresponds to GaAs (AlAs). (b) Scanning-electron-microscope image of an elliptical micropillar. The red (blue) arrow indicates the major (a) axis [minor (b)] axis of the cross section, associated with the vertical (V) [horizontal (H)] polarization. (c) Pump-probe experimental setup. (d) Optical reflectivity of a 4-μm-diameter circular micropillar. (e) Optical reflectivities of an elliptical micropillar with major (red) and minor (blue) axes of 4 and 2 μm, respectively. (f) Optical mode splitting of five micropillars with a minor axis of 4, 2.8, 2.6, 2.4, and 2 μm, while the length of the major axis is 4 μm. (g) Differential reflectivity in the time domain. The inset shows an enlargement of the reflectivity time trace, showing low-amplitude oscillations due to coherent acoustic phonons. (h) Fast Fourier transform of the time trace shown in (g). AOM, acousto-optic modulator; BS, beam splitter; HWP, half-wave plate; PBS, polarizing beam splitter; PD, photodiode; Pol, polarizer; QWP, quarter-wave plate.

top (bottom) DBR is formed by 25 (29) periods of $Ga_{0.9}Al_{0.1}As/Ga_{0.05}Al_{0.95}As$ ($\lambda/4, \lambda/4$). This design constitutes an optophononic resonator confining near-infrared photons at around $\lambda = 900$ nm and acoustic phonons at approximately 18 GHz [13,15,42], with an optical Q factor of approximately 11 000. See Appendix A for further details. Elliptical micropillars are processed from the planar cavity by electron-beam lithography and inductively-coupled-plasma etching. Figure 1(b) shows a scanning-electron-microscope image of a micropillar with an elliptical cross section. Here, we define the major axis as a and the minor axis as b.

The schematics of the pump-probe time-domain Brillouin-scattering technique [26,27], used to study coherent phonon generation and detection, is displayed in Fig. 1(c). Picosecond pulses from a Ti:sapphire laser are split into two linearly polarized beams with orthogonal polarizations (pump and probe) by a polarizing beam splitter. The pump generates phonons via the deformation-potential mechanism. The presence of coherent acoustic phonons in the structure modulates the material's refractive index. The probe beam then detects transient reflectivity changes. By scanning the time delay between the pump and probe beams with a mechanical delay line, we can reconstruct the reflectivity time trace of the structure. Both beams merge at the beam splitter and are coupled to a single-mode fiber. They are focused on the sample to a spot with a diameter of approximately 2.2 μm with an objective lens with a numerical aperture of 0.7. The reflected light is coupled to a different fiber and sent to a fast photodetector. A combination of quarter-wave and half-wave plates is used to manipulate the polarization of the two beams. For the collection, the pump is filtered out by a cross-polarization filtering scheme with a second set of quarter-wave and half-wave plates and a polarizer before the photodetector. The signal is then analyzed by a lock-in amplifier. To observe the optical modes of the elliptical pillars, reflectivity measurements can be performed with the same setup [41]. Broadband light is adapted to the incident path, and the reflected light is sent to a double spectrometer and detected by a charge-coupled device. A removable polarizer is placed in the collection path, before the fiber, to select the polarization of interest. All measurements are performed at room temperature.

Figures 1(d) and 1(e) display the reflectivity spectra of micropillars with a circular ($a = b = 4$ μm) and an elliptical ($a = 4$ μm and $b = 2$ μm) cross section, respectively. The reflectivity of the circular micropillar reveals a cavity mode centered at 902.27 nm, with a full width at half maximum of approximately 0.08 nm. Only one optical mode is present and it has no preferential polarization axis. The eigenfrequency is inversely proportional to the micropillar radius. In the case of the elliptical micropillar, the degeneracy of the eigenfrequency is lifted and we can observe two optical cavity modes in the reflectivity according to each axis of the elliptical cross section and they are conventionally associated with the vertical and horizontal linear polarization for the major axis (a) and the minor axis (b), respectively. The vertical and horizontal modes are at 900.90 and 900.77 nm, respectively, exhibiting a splitting $\Delta\lambda$ of 0.13 nm. In the case of acoustic phonons in the structures studied, due to Poisson's ratio, there are no eigenmodes associated with pure vertical and horizontal polarizations [14]. The frequency of the confined mode is determined mainly by the spacer thickness (see Appendix B). The optical-mode-splitting dependence on the length of the minor axis b (while the length of the major axis a remains constant at 4 μm) is displayed in Fig. 1(f). The splitting increases with decreasing b.

A typical pump-probe time-dependent differential reflectivity is displayed in Fig. 1(g). A rapid change and an exponential decay within approximately 500 ps are present. After removing the low-frequency component and performing a Fourier transform, we observe a peak at around 18.5 GHz in the spectrum [Fig. 1(h)], corresponding to the fundamental mode of the microcavity.

In the pump-probe experiment, we exploit the cross-polarization of the beams combined with the mode splitting of the elliptical pillars. The polarization of the pump beam, which is responsible for the coherent phonon generation, is aligned with the major axis of the micropillar, and therefore it is coupled to the vertical mode of the elliptical pillar. Accordingly, the probe beam, which detects transient reflectivity changes induced by the acoustic phonons, is automatically parallel to the mode along the minor axis (horizontal mode).

B. Model implementation

We propose a simplified 1D model to simulate the pump-probe experiment in elliptical micropillars. We compute the optical reflectivities and the optical and strain fields using the standard transfer-matrix method for multilayered structures, considering the appropriate parameters for electromagnetic waves—refractive index (n) and speed of light (c)—and acoustic waves—mass density (ρ) and speed of sound (v) [9,11,30,43]. To mimic the experimental optical mode splitting of elliptical micropillars, we assume there are two independent structures (corresponding to each axis) for each ellipticity: first, we calculate the reflectivity of the vertical mode (associated with the major axis $a = 4$ μm) at wavelength λ_V; and for the horizontal mode, we tune the overall refractive index of the multilayered structure so that the optical resonance is shifted, and the wavelength difference between the horizontal and vertical modes match the experimental splitting. The reflectivity of the mode along the minor axis for four different cases (4, 2.8, 2.4, and 2 μm) is shown in Fig. 2(a). Note that the reflectivity spectrum for the case $b = a = 4$ μm falls

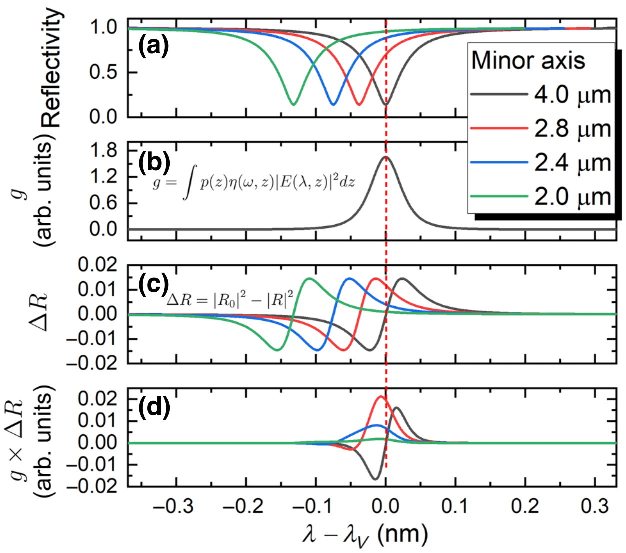

FIG. 2. Simulation of phonon generation and detection in four elliptical micropillars with minor axis $b = 4$ μm (black), 2.8 μm (red), 2.4 μm (blue), and 2 μm (green), whereas the major axis $a = 4$ μm is fixed. (a) Simulated reflectivity of four pillars as a function of optical mode shifting relative to consistent vertical mode. (b),(c) Phonon-generation and phonon-detection spectra, respectively. (d) Product of the generation and detection spectra.

in the circular-micropillar situation, in which the mode is independent of the axis orientation.

The amplitude of the coherent phonon generation $g(\omega, \lambda)$ is given by the overlap integral [9,30]:

$$g(\omega, \lambda) = \int p(z)\eta(\omega, z)|E(\lambda, z)|^2 dz, \qquad (1)$$

where $\omega = 2\pi f$, λ, z, $p(z)$, $\eta(\omega, z)$, and $E(\lambda, z)$ correspond to the acoustic phonon angular frequency, the optical wavelength, the position along the multilayer stacking axis, the material-dependent photoelastic constant—which we assume has a nonzero constant value at the cavity spacer—the acoustic strain field, and the laser electric field, respectively, in which the last two are calculated with the transfer-matrix method. The strain field is calculated at the acoustic resonant frequency. The phonon-generation amplitude as a function of the excitation-laser wavelength at the acoustic resonant frequency $f = 18.5$ GHz is displayed in Fig. 2(b). The peak amplitude centered at λ_V is a consequence of the maximum overlap integral between electric and strain fields.

The detection efficiency, which is independent of the generation process, can be calculated by one assuming there is a photoelastic interaction. The acoustic phonons present in the structure modify the refractive indices, which leads to a differential modification of the optical reflectivity. We consider a perturbative term (Δn) for the refractive index proportional to the product of the strain field at $f = 18.5$ GHz with the photoelastic constant $p(z)$. We then calculate the perturbed optical reflectivity R with the modified strain $n' = n_0 + \Delta n$. Finally, the variation in reflectivity is calculated by [30]

$$\Delta R(\lambda, \omega) = |R_0(\lambda)|^2 - |R(\lambda, \omega)|^2, \qquad (2)$$

where R_0 is the unperturbed reflectivity. The detection process is performed by the probe beam, which is coupled to the horizontal mode; therefore, these calculations are repeated for every minor-axis length, as shown in Fig. 2(c). One can see that the detection efficiency is always zero at the center of the optical cavity mode, and is maximum (with opposite signs) at both slopes.

The product of the phonon-generation and phonon-detection spectra, shown in Fig. 2(d), maps the resulting wavelength-dependent phonon amplitude for each elliptical case. However, the pulsed laser used in the experiment has a spectral Gaussian profile with an associated full width at half maximum of around twice the optical cavity linewidth. Each wavelength component of the laser is then susceptible to a different phonon-generation-detection efficiency. To account for that, we calculate the product of a Gaussian centered at λ_V, related to the laser spectral profile, with the function displayed in Fig. 2(d). The simulated phonon amplitude is then a result of an overlap integral between the laser spectrum and the generation and detection efficiencies. In a circular micropillar, one can predict that the phonon amplitude will be close to zero due to the opposite signs of the detection efficiency, which can be understood as counterphase reflectivity modulation that cancels the signal. In addition, the case with a minor axis of 2.8 μm leads to the strongest signal, and finally, the extreme case of 2 μm leads to a weak phonon signal again, as the horizontal mode is well detuned from the laser.

III. RESULTS AND DISCUSSION

Figure 3 presents the normalized pump-probe phonon amplitude as a function of the splitting between the horizontal and vertical optical modes. The case of zero splitting corresponds to a circular micropillar with a diameter of 4 μm. The error bars are associated with the standard deviation of the amplitude among five measurements on each pillar. The experiment is performed with pump and probe powers of 40 and 100 μW, respectively. The laser is tuned in resonance with the vertical mode so that the phonon-generation efficiency is constant.

For circular micropillars, the phonon amplitude is nearly zero. In this case, the counterphase reflectivity modulation at both slopes of the cavity is equally sensed by the probe, which cancels the signal. By our increasing the ellipticity, the detected phonon signal increases and reaches a maximum amplitude for the pillar with $b = 2.4$ μm. At the other extreme, the splitting of the

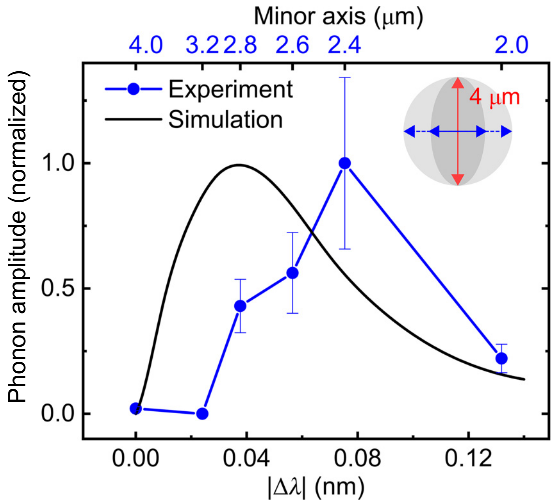

FIG. 3. Normalized amplitude of the phonon signal as a function of the length of the minor axis of the pillars (top axis) and the mode splitting (bottom axis). The experimental and simulation results are presented in blue and black, respectively. The error bars correspond to the standard deviation of five consecutive experiments.

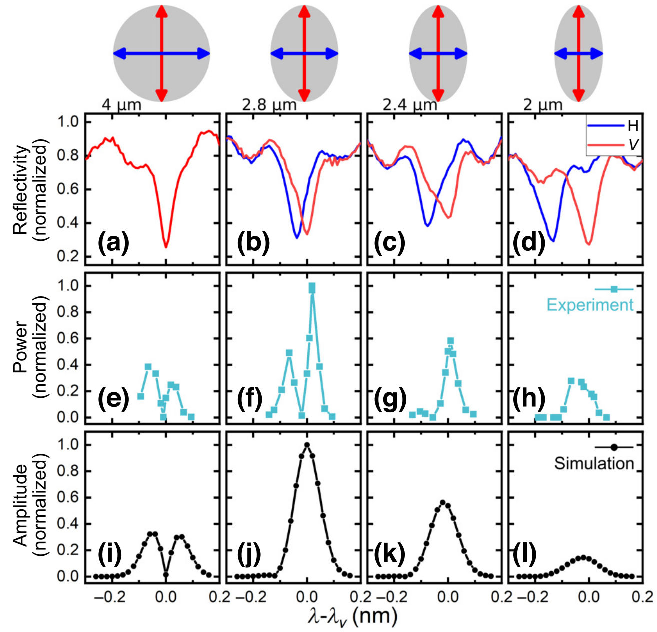

FIG. 4. Wavelength-dependent phonon signal on micropillars. Each column corresponds to one micropillar, as shown at top of the figure. (a)–(d) Experimental reflectivity. (e)–(h) Laser-wavelength dependence of the power of the phonon signal. (i)–(l) Simulated phonon amplitude as a function of laser detuning. H, horizontal polarization; V, vertical polarization.

modes leads to a probe weakly coupled into the horizontal mode, and thus the detected phonon signal decreases. The linewidths of the laser pulse and the optical cavity mode are comparable. This leads to a strongly-wavelength-dependent coherent-phonon-generation-detection process for the highest-phonon-amplitude case. The combination of small laser-wavelength fluctuations with slightly different mode matching in each experiment increases imprecision. Despite the large error bars, the phonon amplitude within the experimental error is still higher than the amplitudes at adjacent ellipticities.

Although the trend is compatible with the predicted trend, with a maximum phonon amplitude in between the two extreme cases, there is a clear offset between the experimental results and the simulation curve shown in Fig. 3, according to the model described in the previous section. The computed values show a maximum phonon amplitude for an elliptical micropillar with $b = 2.8$ μm, with a mode splitting of approximately 0.038 nm, i.e., approximately 0.032 nm less than the measured one. We associate this discrepancy with the warming up of the sample due to the relatively high power of both the pump beam and the probe beam. The warming-up process consists of a change of the index of refraction due to the change in temperature of the sample produced by the absorption of the pump and probe pulses. This heating induces a redshift of the optical cavity mode, changing the optical coupling condition of the probe, and thus its sensitivity [44].

We perform pump-probe experiments as a function of the laser wavelength for four elliptical pillars across the optical cavity modes in steps of approximately 0.01 nm. To minimize warming-up effects, the pump and probe powers are reduced to 30 and 25 μW, respectively, corresponding to respective reductions of 25% and 75%, compared with the previous experiment. For reference, the reflectivity and cross section of the micropillars are shown in Figs. 4(a)–4(d). In Figs. 4(e)–4(h), we present the measured phonon intensity as a function of the laser wavelength. We simulate the laser detuning by shifting the center wavelength of the Gaussian profile that is multiplied by the phonon-generation-detection function. In Figs. 4(i)–4(l), the plots display the phonon amplitude, i.e., the integral of the resulting product, as a function of the laser detuning.

For the circular micropillar [Fig. 4(e)], when there is no symmetry breaking in the cross section, the results are aligned with previously reported results [30,31]. The highest amplitude occurs along the slopes of the optical cavity, indicating that the detection process is directly associated with the modulation of the refractive index of the structure. These results are consistent with the simulations depicted in Fig. 4(i). By our introducing the ellipticity, the shape of the wavelength-dependent phonon amplitude changes. Notably, the intensity now reaches the maximum when the length of the minor axis is 2.8 μm [Fig. 4(f)], as previously expected, which indicates that warming-up effects are less pronounced (see Appendix C). Note that for this specific elliptical cross section, the phonon signal is strongly dependent on the laser wavelength close to the maximum amplitude. A wavelength shift in the response is observed, which might still be associated with a warming up of the sample. When comparing the results with the numerical calculations, displayed in Fig. 4(j), although the position of the maximum amplitude is comparable, we observe a dip in the experimental results, which is not present in the simulations. This dip becomes evident when we simulate intermediate cases between Fig. 4(i) and Fig. 4(j) (see Appendix D). Discrepancies might stem from unaccounted factors such as fabrication imperfections—in the layers' thicknesses during the growth and in the elliptical shape during etching—causing incomplete decoupling of the horizontally polarized and vertically polarized optical cavity modes and reduction of the optical Q factor, or laser instabilities leading to slight detunings between the laser and the optical resonances. Nevertheless, when comparing the ratio between the maximum experimental amplitude from Fig. 4(f) and the maximum experimental amplitude for the circular micropillar [Fig. 4(e)], in which the latter corresponds to the standard procedure of tuning the laser wavelength at the slope of the optical cavity mode, we observe an increase by a factor of approximately 2.6. Theoretically, when comparing Figs. 4(i) and 4(j), we find this factor reaches approximately 3.1. Finally, for the elliptical pillars with $b = 2.4$ μm [Fig. 4(g)] and $b = 2$ μm [Fig. 4(h)], we observe one distinct peak, which matches well with the simulation [Figs. 4(k) and 4(i)].

These results demonstrate the feasibility of engineering more-efficient transduction of acoustic phonons by shaping the elliptical cross section of micropillars for practical applications.

IV. CONCLUSIONS

In this study, we have investigated the unique properties of optophononic micropillar cavities with elliptical cross sections, focusing on enhancing the coherent-phonon-generation and coherent-phonon-detection processes simultaneously. Our findings reveal a significant influence of micropillar ellipticity on phonon signals, demonstrating maximum amplitude at specific major-axis and minor-axis lengths. When comparing the highest signals between elliptical and circular micropillars, we report a theoretical enhancement of a factor of approximately 3.1. This study marks a significant advancement in the development of an efficient ultrahigh-frequency acoustic phonon platform, which is crucial for practical applications in areas such as quantum technologies and data processing.

ACKNOWLEDGMENTS

The authors gratefully acknowledge P. Priya for fruitful discussions and support at an early stage of the project. The authors acknowledge funding from European Research Council Consolidator Grant No. 101045089 (T-Recs). This work was done within the C2N micro nanotechnologies platforms and partly supported by the RENATECH network and the General Council of Essonne. Additional support was provided by the European Commission in the form of the Horizon 2020 Future Emerging Technologies Proactive project No. 824140 (TOCHA), and through a public grant overseen by the Agence Nationale de la Recherche as part of the "Investissements d'Avenir" program (Labex NanoSaclayGrant No. ANR-10-LABX-0035).

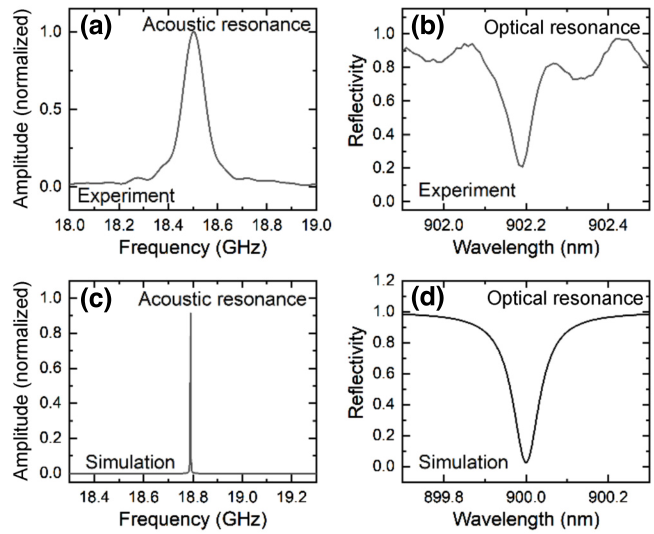

FIG. 5. (a) Fast Fourier transform of the time trace shown in Fig. 1(g). (b) Optical reflectivity of a circular micropillar. (c) Simulation of the phonon-generation-detection spectrum based on the transfer-matrix method and the photoelastic model. (d) Simulated optical reflectivity with use of transfer-matrix method.

APPENDIX A: ACOUSTIC AND OPTICAL MODES

The experimental acoustic and optical modes are displayed in Figs. 5(a) and 5(b). We observe a peak at around 18.5 GHz in the spectrum [Fig. 5(a)], corresponding to the fundamental mode of the microcavity. A reflectivity spectrum of the micropillar with circular cross section with a diameter of 4 μm is presented in Fig. 5(b), featuring the optical cavity at 902.2 nm. The simulated acoustic mode, calculated with the transfer-matrix method and the photoelastic model, and the optical reflectivity, calculated with the transfer-matrix method for electromagnetic waves, are displayed in Figs. 5(c) and 5(d), respectively. The calculated optical and acoustic features have good agreement with the experimental results, apart from small wavelength and frequency shifts due to deviations from the nominal thickness values. The wider linewidth of the experimental phononic mode, compared with the simulation, is due to both the low power used in the experiment, resulting in a decreased temporal signal-to-noise ratio, and the experimental time window of 12 ns, which does not reflect the mode lifetime.

APPENDIX B: DEPENDENCE OF ACOUSTIC MODES ON MICROPILLAR ELLIPTICITY

We study the dependence of the acoustic modes on the micropillar ellipticity in the low-frequency and high-frequency regimes. In the low-frequency regime, the eigenmodes are determined mainly by the lateral size and shape of the structure. We perform finite-element-method simulations with COMSOL MULTIPHYSICS of a simplified model, composed of a 3D approximately-130-nm-thick elliptical GaAs microdisk representing the cavity spacer (Fig. 6). We simulate the eigenfrequencies of the microdisk with different ellipticities, in which the length of the minor axis ranges from 0.4 to 4 μm, whereas the length of the major axis is fixed at 4 μm [Fig. 6(a)]. In the strain profile, for a particular ellipticity of $4 \times 2.8\ \mu\text{m}^2$ (major axis times minor axis), we observe two orthogonal modes at frequencies much lower than the vertically confined acoustic mode [Figs. 6(b) and 6(c)]. In addition, by our increasing the length of the minor axis, an expected decrease of its associated mode frequency is observed, while practically there is no effect for the lower frequency. This is analogous to the electromagnetic case.

In the high-frequency regime, when we analyze the confined acoustic cavity mode, its resonance frequency is determined by the thickness of the spacer. In Fig. 7 we simulate the eigenstates of two micropillars with different cross sections but identical vertical profile. Figure 7 displays the strain profiles of the acoustic mode of micropillars with five DBR periods below and above the spacer for two different cross sections: circular [Fig. 7(a)] and elliptical [Fig. 7(b)]. One can clearly see that the strain profile is almost identical in both cases.

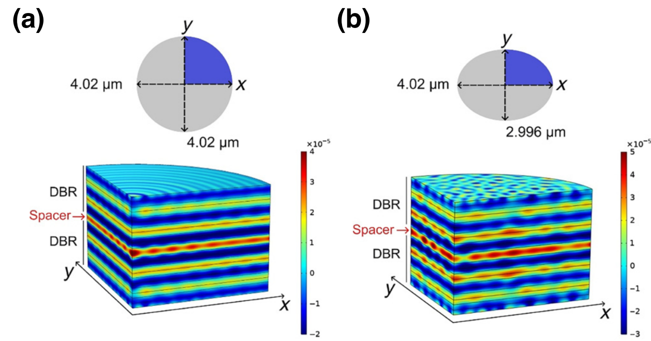

FIG. 7. Volumetric strain profile of the acoustic mode associated with (a) a 4.02-μm-diameter circular micropillar and (b) an elliptical micropillar with major-axis and minor-axis dimensions of 4.02 and 2.996 μm, respectively. The vertical structure of both micropillars is composed of a distributed Bragg reflector of five periods of GaAs/AlAs below and above a GaAs spacer.

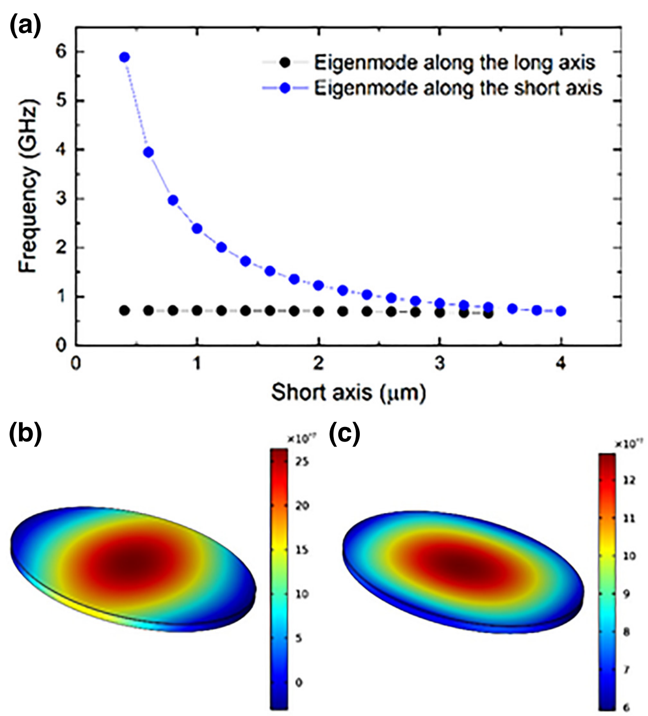

FIG. 6. (a) Frequency dependence of the elliptical microdisk eigenmodes on the length of the minor axis. Two lateral modes are present, associated with each axis. Strain profile of the microdisk with axis dimensions of $4 \times 2.8\ \mu\text{m}^2$ (major axis times minor axis) for the eigenfrequency at (b) 0.91 GHz (minor axis) and (c) 0.68 GHz (major axis).

APPENDIX C: INFLUENCE OF WARMING-UP PROCESSES ON THE COHERENT-PHONON-DETECTION SENSITIVITY

The warming-up process consists of a change in the index of refraction due to the change in the temperature of the sample produced by the absorption of the pump and probe pulses. This heating induces a redshift of the optical cavity mode, changing the optical coupling condition of the probe, and thus its sensitivity. Since the coupling condition depends on the absorption of the laser light, it is important to present the acoustic response at different powers, showcasing different real-life experimental conditions. In Fig. 8 we include information similar to the information depicted in Fig. 3, comparing measurements at high power and low power (both normalized by the maximum amplitude at each power), where the thermal effects are reduced. For the low-power case, we extracted the amplitude of each measurement displayed in Figs. 4(e)–4(h) at the wavelength shifted by approximately 0.02 nm from the center position of the vertical mode (λ_V). This accounts for a general minor offset of the result.

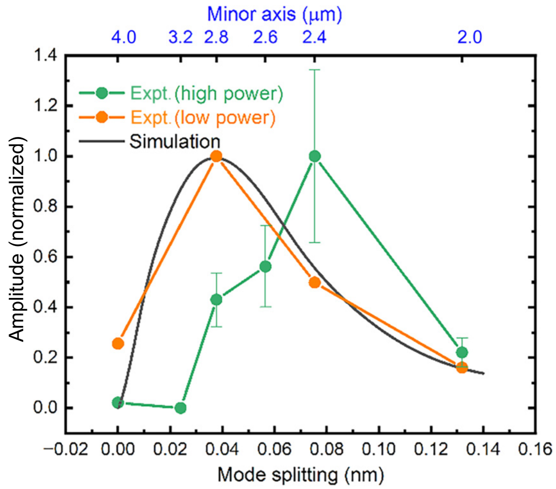

FIG. 8. Normalized amplitude of the phonon signal as a function of the length of the minor axis of the pillars (top axis) and the mode splitting (bottom axis), obtained under experimental conditions of high power (green circles, pump power of 40 μW and probe power of 100 μW) and low power (orange circles, pump power of 30 μW and probe power of 25 μW). The error bars correspond to the fluctuation of five consecutive experiments. The data corresponding to the low power are extracted from each measurement displayed in Figs. 4(e)–4(h) at the wavelength shifted by 0.02 nm from the center position of vertical mode (λ_V). The black curve corresponds to the simulation results.

APPENDIX D: DEPENDENCE OF PHONON-GENERATION-DETECTION AMPLITUDE ON THE MINOR-AXIS LENGTH

Figure 9 displays the simulated phonon amplitude as a function of the laser-wavelength detuning for micropillars with different ellipticities. This shows a more-detailed dependence of the result on the ellipticity, evidencing a remarkable good matching between experiments and simulations. The simulation results clearly reproduce the main trends observed experimentally, including the appearance of a dip in the curve [displayed in Figs. 4(e)– 4(h)].

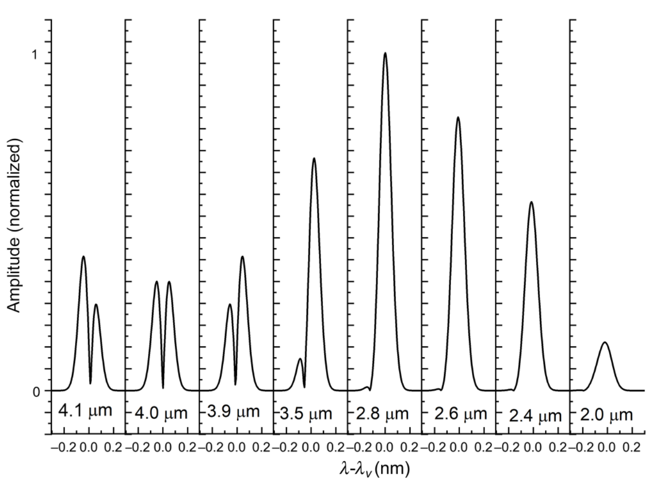

FIG. 9. Simulated wavelength-dependent phonon signal on micropillars with different ellipticities.

[1] P. Priya, E. R. Cardozo de Oliveira, and N. D. Lanzillotti-Kimura, Perspectives on high-frequency nanomechanics, nanoacoustics, and nanophononics, Appl. Phys. Lett. **122**, 140501 (2023).

[2] A. A. Balandin, Nanophononics: Phonon engineering in nanostructures and nanodevices, J. Nanosci. Nanotechnol. **5**, 1015 (2005).

[3] S. Volz, *et al.*, Nanophononics: State of the art and perspectives, Eur. Phys. J. B **89**, 15 (2016).

[4] A. D. O'Connell, M. Hofheinz, M. Ansmann, R. C. Bialczak, M. Lenander, E. Lucero, M. Neeley, D. Sank, H. Wang, M. Weides, J. Wenner, J. M. Martinis, and A. N. Cleland, Quantum ground state and single-phonon control of a mechanical resonator, Nature **464**, 697 (2010).

[5] Y. Chu, P. Kharel, W. H. Renninger, L. D. Burkhart, L. Frunzio, P. T. Rakich, and R. J. Schoelkopf, Quantum acoustics with superconducting qubits, Science **358**, 199 (2017).

[6] U. von Lüpke, Y. Yang, M. Bild, L. Michaud, M. Fadel, and Y. Chu, Parity measurement in the strong dispersive regime of circuit quantum acoustodynamics, Nat. Phys. **18**, 794 (2022).

[7] D. L. Chafatinos, A. S. Kuznetsov, S. Anguiano, A. E. Bruchhausen, A. A. Reynoso, K. Biermann, P. V. Santos, and A. Fainstein, Polariton-driven phonon laser, Nat. Commun. **11**, 4552 (2020).

[8] A. S. Kuznetsov, K. Biermann, A. A. Reynoso, A. Fainstein, and P. V. Santos, Microcavity phonoritons – A coherent optical-to-microwave interface, Nat. Commun. **14**, 5470 (2023).

[9] A. Fainstein and B. Jusserand, in *Light Scattering in Solid IX*, edited by M. Cardona and R. Merlin (Springer, Berlin, Heidelberg, 2007), p. 17.

[10] N. D. Lanzillotti-Kimura, A. Fainstein, A. Huynh, B. Perrin, B. Jusserand, A. Miard, and A. Lemaître, Coherent generation of acoustic phonons in an optical microcavity, Phys. Rev. Lett. **99**, 217405 (2007).

[11] N. D. Lanzillotti-Kimura, A. Fainstein, C. A. Balseiro, and B. Jusserand, Phonon engineering with acoustic nanocavities: Theoretical considerations on phonon molecules, band structures, and acoustic Bloch oscillations, Phys. Rev. B **75**, 024301 (2007).

[12] N. D. Lanzillotti-Kimura, A. Fainstein, B. Jusserand, A. Lemaître, O. Mauguin, and L. Largeau, Acoustic phonon nanowave devices based on aperiodic multilayers: Experiments and theory, Phys. Rev. B **76**, 174301 (2007).

[13] S. Anguiano, A. E. Bruchhausen, B. Jusserand, I. Favero, F. R. Lamberti, L. Lanco, I. Sagnes, A. Lemaître, N. D. Lanzillotti-Kimura, P. Senellart, and A. Fainstein, Micropillar resonators for optomechanics in the extremely high 19–95-GHz frequency range, Phys. Rev. Lett. **118**, 263901 (2017).

[14] F. R. Lamberti, Q. Yao, L. Lanco, D. T. Nguyen, M. Esmann, A. Fainstein, P. Sesin, S. Anguiano, V. Villafañe, A. Bruchhausen, P. Senellart, I. Favero, and N. D. Lanzillotti-Kimura, Optomechanical properties of GaAs/AlAs micropillar resonators operating in the 18 GHz range, Opt. Express **25**, 24437 (2017).

[15] M. Esmann, F. R. Lamberti, A. Harouri, L. Lanco, I. Sagnes, I. Favero, G. Aubin, C. Gomez-Carbonell, A. Lemaître, O. Krebs, P. Senellart, and N. D. Lanzillotti-Kimura, Brillouin scattering in hybrid optophononic Bragg micropillar resonators at 300 GHz, Optica **6**, 854 (2019).

[16] D. Bajoni, P. Senellart, E. Wertz, I. Sagnes, A. Miard, A. Lemaître, and J. Bloch, Polariton laser using single micropillar GaAs-GaAlAs semiconductor cavities, Phys. Rev. Lett. **100**, 047401 (2008).

[17] N. Carlon Zambon, Z. Denis, R. De Oliveira, S. Ravets, C. Ciuti, I. Favero, and J. Bloch, Enhanced cavity optomechanics with quantum-well exciton polaritons, Phys. Rev. Lett. **129**, 093603 (2022).

[18] P. Senellart, G. Solomon, and A. White, High-performance semiconductor quantum-dot single-photon sources, Nat. Nanotechnol. **12**, 1026 (2017).

[19] K. O'Brien, N. D. Lanzillotti-Kimura, J. Rho, H. Suchowski, X. Yin, and X. Zhang, Ultrafast acousto-plasmonic control and sensing in complex nanostructures, Nat. Commun. **5**, 4042 (2014).

[20] N. D. Lanzillotti-Kimura, K. P. O'Brien, J. Rho, H. Suchowski, X. Yin, and X. Zhang, Polarization-controlled coherent phonon generation in acoustoplasmonic metasurfaces, Phys. Rev. B **97**, 235403 (2018).

[21] H. Baida, A. Crut, P. Maioli, T. B. Nguyen, D. H. Nguyen, N. D. Fatti, and F. Vallée, Optical detection and femtosecond spectroscopy of a single nanoparticle, Adv. Nat. Sci.: Nanosci. Nanotechnol. **2**, 035011 (2011).

[22] H. Baida, D. Mongin, D. Christofilos, G. Bachelier, A. Crut, P. Maioli, N. Del Fatti, and F. Vallée, Ultrafast nonlinear optical response of a single gold nanorod near its surface plasmon resonance, Phys. Rev. Lett. **107**, 057402 (2011).

[23] R. Berte, F. Della Picca, M. Poblet, Y. Li, E. Cortés, R. V. Craster, S. A. Maier, and A. V. Bragas, Acoustic far-field hypersonic surface wave detection with single plasmonic nanoantennas, Phys. Rev. Lett. **121**, 253902 (2018).

[24] M. Poblet, R. Berté, H. D. Boggiano, Y. Li, E. Cortés, G. Grinblat, S. A. Maier, and A. V. Bragas, Acoustic coupling between plasmonic nanoantennas: Detection and directionality of surface acoustic waves, ACS Photonics **8**, 2846 (2021).

[25] B. Castillo López de Larrinzar, C. Xiang, E. R. Cardozo de Oliveira, N. D. Lanzillotti-Kimura, and A. García-Martín, Towards chiral acoustoplasmonics, Nanophotonics **12**, 1957 (2023).

[26] C. Thomsen, J. Strait, Z. Vardeny, H. J. Maris, J. Tauc, and J. J. Hauser, Coherent phonon generation and detection by picosecond light pulses, Phys. Rev. Lett. **53**, 989 (1984).

[27] C. Thomsen, H. T. Grahn, H. J. Maris, and J. Tauc, Surface generation and detection of phonons by picosecond light pulses, Phys. Rev. B **34**, 4129 (1986).

[28] P. Ruello and V. E. Gusev, Physical mechanisms of coherent acoustic phonons generation by ultrafast laser action, Ultrasonics **56**, 21 (2015).

[29] N. D. Lanzillotti-Kimura, A. Fainstein, B. Perrin, B. Jusserand, L. Largeau, O. Mauguin, and A. Lemaitre, Enhanced optical generation and detection of acoustic nanowaves in microcavities, Phys. Rev. B **83**, 201103 (2011).

[30] N. D. Lanzillotti-Kimura, A. Fainstein, B. Perrin, and B. Jusserand, Theory of coherent generation and detection of THz acoustic phonons using optical microcavities, Phys. Rev. B **84**, 064307 (2011).

[31] S. Anguiano, A. E. Bruchhausen, I. Favero, I. Sagnes, A. Lemaître, N. D. Lanzillotti-Kimura, and A. Fainstein, Optical cavity mode dynamics and coherent phonon generation in high-Q micropillar resonators, Phys. Rev. A **98**, 013816 (2018).

[32] E. Péronne, E. Charron, S. Vincent, S. Sauvage, A. Lemaître, B. Perrin, and B. Jusserand, Two-color femtosecond strobe lighting of coherent acoustic phonons emitted by quantum dots, Appl. Phys. Lett. **102**, 043107 (2013).

[33] O. Ortiz, F. Pastier, A. Rodriguez, P. Priya, A. Lemaitre, C. Gomez-Carbonell, I. Sagnes, A. Harouri, P. Senellart, V. Giesz, M. Esmann, and N. D. Lanzillotti-Kimura, Fiber-integrated microcavities for efficient generation of coherent acoustic phonons, Appl. Phys. Lett. **117**, 183102 (2020).

[34] B. Gayral, J. M. Gérard, B. Legrand, E. Costard, and V. Thierry-Mieg, Optical study of GaAs/AlAs pillar microcavities with elliptical cross section, Appl. Phys. Lett. **72**, 1421 (1998).

[35] D. M. Whittaker, P. S. S. Guimaraes, D. Sanvitto, H. Vinck, S. Lam, A. Daraei, J. A. Timpson, A. M. Fox, M. S. Skolnick, Y.-L. D. Ho, J. G. Rarity, M. Hopkinson, and A. Tahraoui, High Q modes in elliptical microcavity pillars, Appl. Phys. Lett. **90**, 161105 (2007).

[36] K. Sebald, M. Seyfried, S. Klembt, and C. Kruse, Optical properties of photonic molecules and elliptical pillars made of ZnSe-based microcavities, Opt. Express **19**, 19422 (2011).

[37] H. Wang, *et al.*, Towards optimal single-photon sources from polarized microcavities, Nat. Photonics **13**, 770 (2019).

[38] A. Daraei, A. Tahraoui, D. Sanvitto, J. A. Timpson, P. W. Fry, M. Hopkinson, P. S. S. Guimarães, H. Vinck, D. M. Whittaker, M. S. Skolnick, and A. M. Fox, Control of polarized single quantum dot emission in high-quality-factor microcavity pillars, Appl. Phys. Lett. **88**, 051113 (2006).

[39] S. Reitzenstein, C. Böckler, A. Löffler, S. Höfling, L. Worschech, A. Forchel, P. Yao, and S. Hughes, Polarization-dependent strong coupling in elliptical high-Q micropillar cavities, Phys. Rev. B **82**, 235313 (2010).

[40] S. Gerhardt, M. Deppisch, S. Betzold, T. H. Harder, T. C. H. Liew, A. Predojević, S. Höfling, and C. Schneider, Polarization-dependent light-matter coupling and highly indistinguishable resonant fluorescence photons from quantum dot-micropillar cavities with elliptical cross section, Phys. Rev. B **100**, 115305 (2019).

[41] A. Rodriguez, P. Priya, E. R. Cardozo De Oliveira, A. Harouri, I. Sagnes, F. Pastier, L. Le Gratiet, M. Morassi,

A. Lemaître, L. Lanco, M. Esmann, and N. D. Lanzillotti-Kimura, Brillouin scattering selection rules in polarization-sensitive photonic resonators, ACS Photonics **10**, 1687 (2023).

[42] O. Ortiz, P. Priya, A. Rodriguez, A. Lemaitre, M. Esmann, and N. D. Lanzillotti-Kimura, Topological optical and phononic interface mode by simultaneous band inversion, Optica **8**, 598 (2021).

[43] O. Matsuda and O. B. Wright, Reflection and transmission of light in multilayers perturbed by picosecond strain pulse propagation, J. Opt. Soc. Am. B **19**, 3028 (2002).

[44] P. Sesin, P. Soubelet, V. Villafañe, A. E. Bruchhausen, B. Jusserand, A. Lemaître, N. D. Lanzillotti-Kimura, and A. Fainstein, Dynamical optical tuning of the coherent phonon detection sensitivity in DBR-based GaAs optomechanical resonators, Phys. Rev. B **92**, 075307 (2015).